J. Plasma Phys. (2020), *vol.* 86, 905860304 © The Author(s), 2020.
Published by Cambridge University Press
doi:10.1017/S0022377820000379

Towards laser ion acceleration with holed targets

Prokopis Hadjisolomou[1,†], **S. V. Bulanov**[1,2] **and G. Korn**[1]

[1]Institute of Physics of the ASCR, ELI-Beamlines project, Na Slovance 2, 18221 Prague, Czech Republic

[2]National Institutes for Quantum and Radiological Science and Technology (QST), Kansai Photon Science Institute, 8-1-7 Umemidai, Kizugawa, Kyoto 619-0215, Japan

(Received 20 March 2020; revised 14 April 2020; accepted 15 April 2020)

Although the interaction of a flat foil with currently available laser intensities is now considered a routine process, during the last decade, emphasis has been given to targets with complex geometries aiming at increasing the ion energy. This work presents a target geometry where two symmetric side holes and a central hole are drilled into the foil. A study of the various side-hole and central-hole length combinations is performed with two-dimensional particle-in-cell simulations for polyethylene targets and a laser intensity of 5.2×10^{21} W cm^{-2}. The holed targets show a remarkable increase of the conversion efficiency, which corresponds to a different target configuration for electrons, protons and carbon ions. Furthermore, diffraction of the laser pulse leads to a directional high energy electron beam, with a temperature of ∼40 MeV, or seven times higher than in the case of a flat foil. The higher conversion efficiency consequently leads to a significant enhancement of the maximum proton energy from holed targets.

Key words: intense particle beams, plasma simulation

1. Introduction

During the last decades the chirped pulse amplification method (Strickland & Mourou 1985; Mourou, Tajima & Bulanov 2006) enabled laser systems to undergo a rapid power increase. Once the laser intensity exceeds $\sim 10^{18}$ W cm^{-2} then an isotropic proton emission is observed from the laser interaction with a flat foil (Maksimchuk *et al.* 2000), with proton energies exceeding 1 MeV. Recently, two groups approached the 100 MeV proton energy threshold (Kim *et al.* 2016; Higginson *et al.* 2018) by using a $\sim 5 \times 10^{20}$ W cm^{-2} intensity laser but at the cost of using nanometre-thickness targets which hardly survive the interaction with the finite contrast prepulse of multi-PW laser systems available in the near future (Rus *et al.* 2011; Zamfir 2012; Bashinov *et al.* 2014; Zou *et al.* 2015).

In contrast with conventionally accelerated proton beams, laser-driven proton beams contain a high number of particles generated in a time comparable to the laser pulse duration, although the divergence of the beam is of ∼30° full angle (Daido, Nishiuchi & Pirozhkov 2012; Macchi, Borghesi & Passoni 2013). However, the reduced cost of

† Email address for correspondence: Prokopis.Hadjisolomou@eli-beams.eu

https://doi.org/10.1017/S0022377820000379 Published online by Cambridge University Press

laser-driven proton beams make them extremely attractive to several existing and/or proposed applications, including the fast ignition of thermonuclear fusion targets (Roth *et al.* 2001; Atzeni, Temporal & Honrubia 2002), hadron therapy (Bulanov & Khoroshkov 2002; Bulanov *et al.* 2004; Murakami *et al.* 2008; Bulanov *et al.* 2014; Kurup *et al.* 2019), isotope production (Santala *et al.* 2001), material sciences (Boody *et al.* 1996) and proton imaging (Borghesi *et al.* 2002, 2003). Specifically, for cancer therapy, ∼250 MeV protons are required to treat a patient, setting a socially accepted minimum proton energy boundary.

A laser beam that mimics the planned High-Repetition-Rate Advanced Petawatt Laser System (HAPLS) in the Extreme Light Infrastructure (ELI) Beamlines (Rus *et al.* 2011), Czech Republic, is assumed for studying the processes discussed in this work. It is estimated that HAPLS will deliver 30 J energy within 27 fs pulse duration at full width half-maximum (FWHM), resulting in a peak power of 1 PW, while the central wavelength, λ, of the laser radiation equals 815 nm. The focal spot diameter is assumed to be 4.75 μm FWHM, which corresponds to a peak intensity of 5.2×10^{21} W cm^{-2}. The resulting amplitude of the maximum electric field is 1.98×10^{14} V m^{-1} (corresponding to a dimensionless amplitude, α_0, of ∼50) and its spatial extent of 6.72 μm FWHM, equals $\sim 8\lambda$.

1.1. *Acceleration mechanisms*

The most well-known laser driven ion acceleration mechanism is the target normal sheath acceleration (TNSA) (Wilks *et al.* 2001; Passoni, Bertagna & Zani 2010; Daido *et al.* 2012; Macchi *et al.* 2013) which dominates at intensities of 10^{20} W cm^{-2} and requires the incidence of a finite contrast laser pulse on a thick (in the micrometre range) flat foil, where the electron number density of the target is higher than the critical electron number density, n_{cr}. Due to the laser–foil interaction, a hot electron population is created with a fraction of it permanently escaping the target. As a consequence of the electron ejection, a longitudinal electric field is established on the target rear surface along with an expanding plasma cloud. Since protons are present on the target as contaminants, they are favourably accelerated due to their high charge to mass ratio, resulting in a spectrum characterised by a double temperature and a sharp cutoff energy.

Once the laser intensity reaches 10^{21} W cm^{-2} the radiation pressure acceleration (RPA) mechanism (Esirkepov *et al.* 2004; Klimo *et al.* 2008; Robinson *et al.* 2008; Bulanov *et al.* 2016) becomes important, where its experimental indications have already been observed (Kim *et al.* 2016; Higginson *et al.* 2018). The RPA mechanism is based on the concept of the relativistic mirrors, where the radiation pressure of the laser pulse pushes the foil (in the interaction region) as a whole. The energy of the pulse is transferred to the foil due to reflection by the co-moving foil mirror. The RPA mechanism requires a circularly polarised laser to be effective, while for a 1 PW laser then nanometre-thick foils are required (Kim *et al.* 2016; Higginson *et al.* 2018). One drawback of the RPA mechanism is that it requires high laser contrast for the foil not to be destroyed by the prepulse prior to the arrival of the main pulse. In the present work only linear polarisation is used and the RPA mechanism is not involved.

If the laser is able to extract almost all electrons from a foil region, then the Coulomb explosion (CE) acceleration mechanism (Bulanov *et al.* 2008; Morita *et al.* 2008; Ogura *et al.* 2012) occurs. Several requirements must be met for CE to be effective, such as a high laser contrast and an optimum target thickness, depending

https://doi.org/10.1017/S0022377820000379 Published online by Cambridge University Press

on the pulse parameters and target density. In order for the CE mechanism to occur, electrons must be ejected within a duration defined by the electron ejection time and the ion response time. Approximately, only electrons within the focal spot contribute to CE. The sudden electron ejection leaves the target with a positively charged ion core. The strong repulsive forces between ions lead to an explosion of the ion core, where the ion spectrum is characterised by a non-thermal distribution. The maximum ion energy is proportional to the maximum electrostatic potential value within the ion core prior the explosion.

If the target has an electron number density near the critical electron number density for relativistically intense electromagnetic waves, $n_{\mathrm{cr}}^{\mathrm{rel}}$, then the incident pulse can channel through the target setting the basis for the magnetic vortex acceleration mechanism (MVA) (Bulanov & Esirkepov 2007; Yogo *et al.* 2008; Bulanov *et al.* 2010*b*; Park *et al.* 2019). Once the pulse exits the target then a quasi-static magnetic field is established, related with the vortex trajectories of electrons in that region. The resulting magnetic field sustains a longitudinal electric field, which is responsible for ion acceleration.

1.2. *Structured targets and holed-target geometry*

Not long after the first MeV laser generated protons were demonstrated by laser irradiation of flat foils, simulations proposed that a curved foil could collimate the proton beam (Bulanov *et al.* 2000; Sentoku *et al.* 2000; Wilks *et al.* 2001) and an experimental demonstration came soon after (Patel *et al.* 2003), setting the new path of laser irradiated microstructured targets. A few notable target proposals include a foil doped with a proton-rich region (Bulanov & Khoroshkov 2002; Esirkepov *et al.* 2002; Schwoerer *et al.* 2006), a hollow microsphere (Burza *et al.* 2011), foils with solid microspheres attached on their front surface (Klimo *et al.* 2011; Margarone *et al.* 2012), foils attached to hollow cones (Bartal *et al.* 2012; Qiao *et al.* 2013), foils with a series of microslits (Nagashima *et al.* 2013; Kawata *et al.* 2014), atomic clusters (Ditmire *et al.* 1997), microwires developed on the target front surface (Jiang *et al.* 2016; Bargsten *et al.* 2017; Rocca *et al.* 2017) and laser irradiated microtubes/microchannel plates (Ji *et al.* 2016; Ji, Snyder & Shen 2019; Snyder *et al.* 2019). Fabrication of microstructures is now considered a routine process and features of $\sim$100 nm can be created by direct laser writing (Fischer & Wegener 2013).

Here, we propose an innovative holed-target geometry where a central hole is drilled into a 1 μm thick polyethylene (Bamberger & Tschirner 1900) foil, centred on the laser focal spot. In addition, two side holes are drilled on the two-dimensional (2-D) foil geometry, symmetrically to the central hole, as shown on the right side of figure 1. The central-hole radius, side-hole inner edge and side-hole outer edge correspond to radii of R_0, R_1 and R_2 respectively, as labelled in figure 1. The foil segment corresponding to a length of R_1–R_0 is called the inner segment (defined as f) and the segment extending from R_2 to ∞ is called the outer segment. The extent of the central-hole radius (defined as $g/2$), the side-hole extent (defined as h) and the inner-segment extent equal a length of 4λ, meaning that the electric field amplitude (Gaussian with 4.75 μm FWHM) at the interaction point and at R_2 have a ratio of 2. The targets considered in the present work cover all combinations of central-hole radius and side-hole extent. From these combinations, since the length sum of the target components (ignoring the outer segment) is 8λ the effect of the inner-segment length can also be extracted. Although the target holes are adjusted to a focal spot with dimensions usually used in laser-proton acceleration experiments, a larger spot (Steinke *et al.* 2020) allows more flexibility on the dimension of the holes.

https://doi.org/10.1017/S0022377820000379 Published online by Cambridge University Press

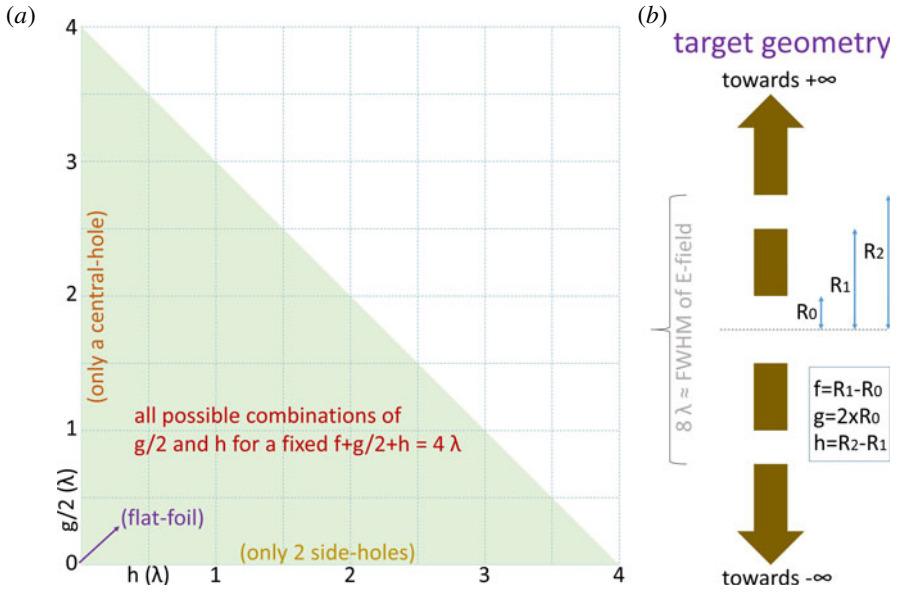


FIGURE 1. (*a*) The green orthogonal triangular area contains the combinations of the central-hole radius and the side-holes' extent, where the length sum of the central hole, the two side holes and the two inner segments equals 8λ. The base and the height of the triangle correspond to HT2SH and HT1CH respectively. The intersection of the two catheti corresponds to a flat foil and the hypotenuse is a sub-case of the holed-target geometry where the two inner segments are removed. (*b*) Schematic representation of a sampled holed target used in the simulations. The target consists of a central hole, defined as g, two side holes, each represented by h, two inner segments, each noted as f, and two outer segments which extend to infinity.

A graphical representation of all possible holed-target geometries if the condition $f + g/2 + h = 4\lambda$ is met is shown on the left side of figure 1, where only the green triangle corresponds to allowed combinations of the extent of central-hole and the extent of the side-holes. Notably, the general holed-target geometry corresponds to two significantly simplified geometries, one at the base and one at the height of the triangle. If one considers only the combinations at the base of the triangle then the target transforms to a centred mass-limited (ML) target plus an outer segment, named the holed target with 2 side holes (HT2SH); if the combinations at the height of the triangle are considered then the target corresponds to a flat foil with a hole in the centre, named the holed target with 1 central hole (HT1CH). The intersection of the base and height of the triangle correspond to a flat foil. All cases along the hypotenuse of the triangle correspond to the same case as a holed target (where the inner segments are removed) regardless of the value of either g or h as long as their sum is 4λ. The only exception is presented in § 3.5 for a HT2SH, where the central foil radius is kept at 0.5λ and the side-holes' extent is gradually increased.

2. Simulations

The results of this work are obtained through the 2-D version of EPOCH (Arber *et al.* 2015) particle-in-cell (PIC) code. The EPOCH version 4.17.19 is compiled with the Higuera–Cary (Higuera & Cary 2017; Ripperda *et al.* 2018) instead of the default

https://doi.org/10.1017/S0022377820000379 Published online by Cambridge University Press

Boris solver (Boris 1970; Ripperda *et al.* 2018). Protons with a velocity exceeding $0.5c$ (where c is the speed of light) and electrons approaching c are expected. Therefore, the use of the Higuera–Cary solver is necessary to simultaneously preserve volume and the $\boldsymbol{E} \times \boldsymbol{B}$ velocity, where $\boldsymbol{E}$ and $\boldsymbol{B}$ is the electric and magnetic field vector respectively (Higuera & Cary 2017). In the present work, although a spectrum comparison of the two solvers exhibits minor differences for protons, the electron spectra are significantly different.

A combination of three overlapping particle species is used, namely electrons, protons (H) and carbon ions (C), consisting a polyethylene foil with a mass density of 0.93 g cm^{-3} and a chemical formula of $(C_2H_4)_n$, where the subscript n is an integer and denotes a macroscopic chain. Electrons, protons and C are assigned to a mass of 1, 1836.15 and 12×1836.15 times the electron rest mass, a charge of -1, 1 and 6 times the elementary charge and a number density of 3.2×10^{23} cm^{-3}, 8×10^{22} cm^{-3} and 4×10^{22} cm^{-3}, respectively. All holed targets are 1 μm thick, with the location and extent of the three holes varying in each simulation.

The simulations use 'open' boundaries in all directions apart the negative (left) x-boundary, which is set to 'simple laser' allowing the launch of a laser pulse from it. The 'open' boundaries allow both fields and particles reaching the box boundary to freely exit the simulation, although the simulation box is large enough to ensure that neither particles nor fields escaped within the simulation time. The laser pulse is launched along the target normal (along $\hat{\boldsymbol{x}}$), following the focusing equations of a Gaussian beam (Siegman 1986), focused at the (0, 0). The laser is P-polarised with a wavelength of 815 nm. The electric field on the focus is described by a Gaussian spatial profile of $\sqrt{2} \times 4.75$ μm FWHM (equal to $\sim 8\lambda$) and a temporal profile of 27 fs FWHM (equal to $\sim 10\lambda$), where the temporal profile is delayed by two standard deviations, σ (where for a Gaussian, σ equals $[2\sqrt{2\ln(2)}]^{-1}$ FWHM), in order for the rising pulse profile to be accurately generated. All simulations use a peak intensity of 5.2×10^{21} W cm^{-2}.

The simulations are performed on the ECLIPSE cluster, using for each simulation 36 nodes with 16 processors per node, where these processors are distributed to a square arrangement of 24×24. To avoid numerical heating by the open boundaries, the dimensions of the simulation box in each direction are set to 122.88 μm × 122.88 μm. The length of each cell in each direction is 10 nm, which approximately equals the skin depth of polyethylene by ignoring the correction due to the relativistically intense electromagnetic waves, while by considering the relativistic correction then the skin depth becomes more than five times larger than the cell size (56 nm). Therefore, each dimension corresponds to 3×2^{12} cells and 9×2^{25} macroparticles are assigned to each specie. By considering that macroparticles are assigned only to cells with non-zero density, initially each cell contains $\sim$40 macroparticles, with the exact number depending on the holes of each holed target. By considering that the laser pulse needs $\sim$200 fs to reach the focal spot at the centre of the box, during the initial 160 fs evolution of particles is disabled to approximately half the computational time. Each simulation runs for 400 fs with 21199 steps (time-step multiplier factor of 0.8), with a time step equal $\sim$1.77 times the cell size over c.

3. Results and discussion

This section provides a detailed description of the results of the general holed-target geometry simulations. Initially, § 3.1 explains how the initial Gaussian pulse profile is rearranged in space after being diffracted and/or reflected by a holed target.

https://doi.org/10.1017/S0022377820000379 Published online by Cambridge University Press

Following this, § 3.2 emphasises electron ejection and propagation following the laser–target interaction, along with the resulting charge separation. In addition, § 3.2 quantifies the amount of laser energy transferred to the target particles. In § 3.3 the acceleration of protons and carbon ions is studied for the general holed-target configuration. Emphasis on the electron and proton spectra extracted from two limit cases of HT2SH and HT1CH is given in § 3.4. The results close with § 3.5, where a transition from the holed-target geometry to a ML target is made.

3.1. *Diffracted fields*

Every laser interaction with a general target geometry results in the same laser energy rearrangement, where a portion of the laser energy is transferred to the target particles (§ 3.2), a small portion is captured by the target as a surface field (Quinn *et al.* 2009; Tokita *et al.* 2015), a third portion is reflected and a fourth portion is transmitted towards the laser propagation direction. In general, the holed-target geometry consists of an infinite flat foil on which three gaps are created. Therefore, it can be described by the theory of diffraction and interference of a planar wave by multiple slits (Born & Wolfl 1999).

However, although a theoretical model can predict the evolution of the laser field after the interaction with the polyethylene foil, several assumptions make a precise analytical prediction hardly possible. Although analytical solutions of the diffracted intensity do exist for an infinite planar wave incident on multiple slits, in our case the pulse has a spatial Gaussian envelope. Furthermore, during the laser–target interaction the target geometry is gradually altered, meaning that the final field configuration is not a result of a single diffraction and interference behaviour. Therefore, the complex field configuration is accurately obtained only through simulations.

The resulting field evolution is shown in figure 2, where the upper half corresponds to a HT1CH with a central hole of 5λ and the lower half to a HT2SH with two side holes of 3.5λ. In both cases, due to the large extent of the holes (large fraction of the pulse spatial profile), most of the laser pulse is transmitted through the target forming an approximately predictable diffraction pattern. The extent of the diffraction effect can be better visualised by considering the longitudinal component of the electric field, E_x, which although initially absent, appears once the pulse passes through the holed target. Notably, a strong E_x field is created in the area between the central hole of the HT1CH. The diffracted field intensity, I, is approximated by the diffraction of a plane wave from a single slit,

$$I = I_0 \left[\mathrm{sinc}\left(\frac{\pi\alpha}{\lambda}\sin(\theta)\right)\right]^2. \tag{3.1}$$

Here, I_0 is the intensity of the assumed plane wave, α is the slit opening and θ is the angle at which the diffracted intensity is estimated. In agreement with the low divergence in figure 2, for 5λ the intensity at FWHM is associated with an angle of $\sim 5^\circ$. Additionally, an even stronger E_x appears on the rear surface of the inner segment of the HT2SH. Notably, E_x in both cases has a duration approximately equal to the laser pulse duration.

Since the laser spatial extent is larger than the holes' extent, a portion of the pulse is reflected by the front target surface. The reflection is not identical for all holed-target configurations, resulting in various complex interference patterns. The final picture is further complicated since the interference can be either constructive or destructive as time evolves. In the case of a HT1CH and a large hole to wavelength

https://doi.org/10.1017/S0022377820000379 Published online by Cambridge University Press

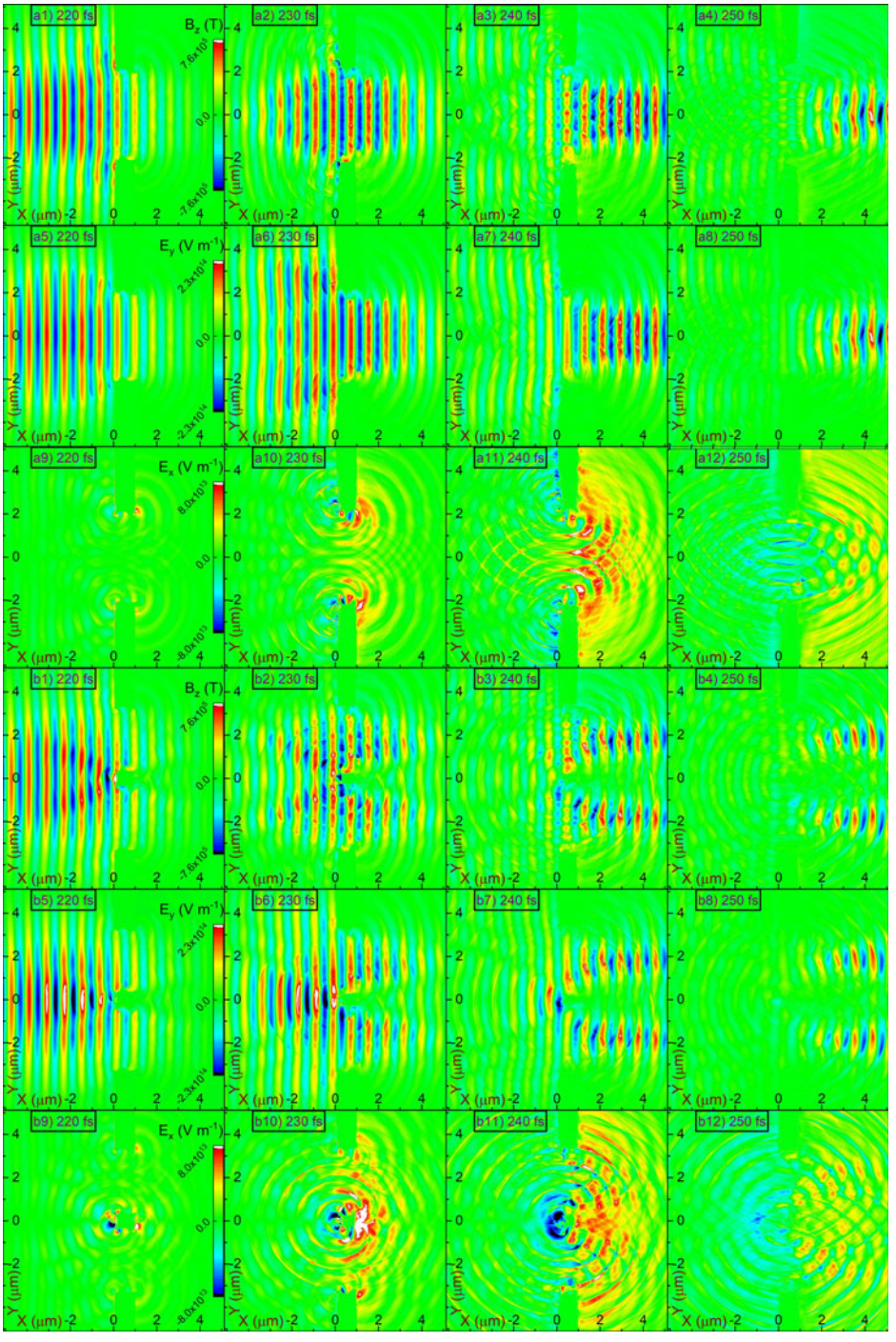


FIGURE 2. Evolution of the magnetic (B_z) and electric (E_y and E_x) field components corresponding to a ($a1$–$a12$) HT1CH with a central hole of 5λ and ($b1$–$b12$) HT2SH with two side holes of 3.5λ.

https://doi.org/10.1017/S0022377820000379 Published online by Cambridge University Press

ratio, interference is not important since practically only the edges of the pulse are reflected. However, for a HT2SH, the central part of the pulse faces a solid inner segment. Therefore, if the inner segment is large enough, the pulse is reflected in a manner similar to reflection from a flat foil. The destructive interference of the magnetic field and constructive interference of the electric field can be seen in figures 2(*b*2) and 2(*b*6) respectively, where a dimmer region of the magnetic field is accompanied by a brighter region of the electric field.

3.2. *Energy transfer, electron evolution and charge separation*

When the rising front of the laser pulse (assumed zero for distances greater than two standard deviations from the pulse peak) reaches the holed target, it is reflected at the locations where inner segments and outer segments exist. However, due to the initially low field amplitude of the pulse rising front (approximately one order of magnitude less than the peak), the field penetrates the target at a depth approximately given by the skin depth of polyethylene (it is equal to $\sim$10 μm) creating a hot electron population. At a time of $\sim$23 fs the electric field on target gets its peak value, penetrating at $\sim$56 μm within the target, further heating electrons.

The initial hot electron distribution eventually leads to several distinct populations. The largest population corresponds to a hot electron cloud refluxing the target, where this behaviour is known as electron 'stochastic heating' (Bulanov *et al.* 2015; Yogo *et al.* 2015, 2017). In our case, these electrons are visualised as the small blue dot in figure 3, at the centre of each image. Another electron fraction moves along the foil in both directions, following a portion of the laser field trapped by the foil and propagating outwards. These electrons have been observed experimentally in cases where the laser pulse had a large incidence angle on a flat foil and a strong electron signal was observed as originating from the foil edges (Li *et al.* 2006; Mao *et al.* 2012; Wang *et al.* 2013). A similar effect was observed by wires directly interacting with a laser pulse (Tokita *et al.* 2011; Nakajima *et al.* 2013; Tokita *et al.* 2015).

A third electron fraction escapes the target as seen by the highest energy electrons in figure 4. Notably, the spatial distribution of the mean electron kinetic energy partially overlaps with the spatial distribution of E_x, as seen by comparing figure 3 with figure 2. This effect is mentioned as 'electron capture' by the laser field (Wang *et al.* 1998; Zhu *et al.* 1998; Wang *et al.* 2001; Braenzel *et al.* 2017), where similar electron patterns are observed in Bulanov *et al.* (2002, 2010*a*). Therefore, those captured electrons are continuously accelerated for as long as they are kept in phase with the pulse (Wang *et al.* 2001; Bulanov *et al.* 2002).

For HT1SH the electron mean energy contours (see figure 4*a*) do not completely correspond to the field spatial distributions (see figure 2*a*). The partial overlap of the two patterns is due to the lack of an inner segment, since the produced electrons originate only from the edges of the pulse. On the other hand, for HT2SH, a plethora of electrons are ejected from the inner segment. That behaviour is also related to the different extents of the hot electron cloud. If no inner segment exists in the path of the pulse then less electrons recirculate the interaction region, as indicated by the reduced size of the central blue dot at the first column and outer diagonal in figure 3, where it is also realised by comparing figure 4(*a*4) with figure 4(*b*4).

The distinction of the several electron populations in combination with the holed-target geometries explain the form of all images grouped in figure 3. In the case of a flat foil (see the intersection of the catheti in figure 3), most of the laser pulse is reflected, capturing a portion of hot electrons driving them to hundreds

https://doi.org/10.1017/S0022377820000379 Published online by Cambridge University Press

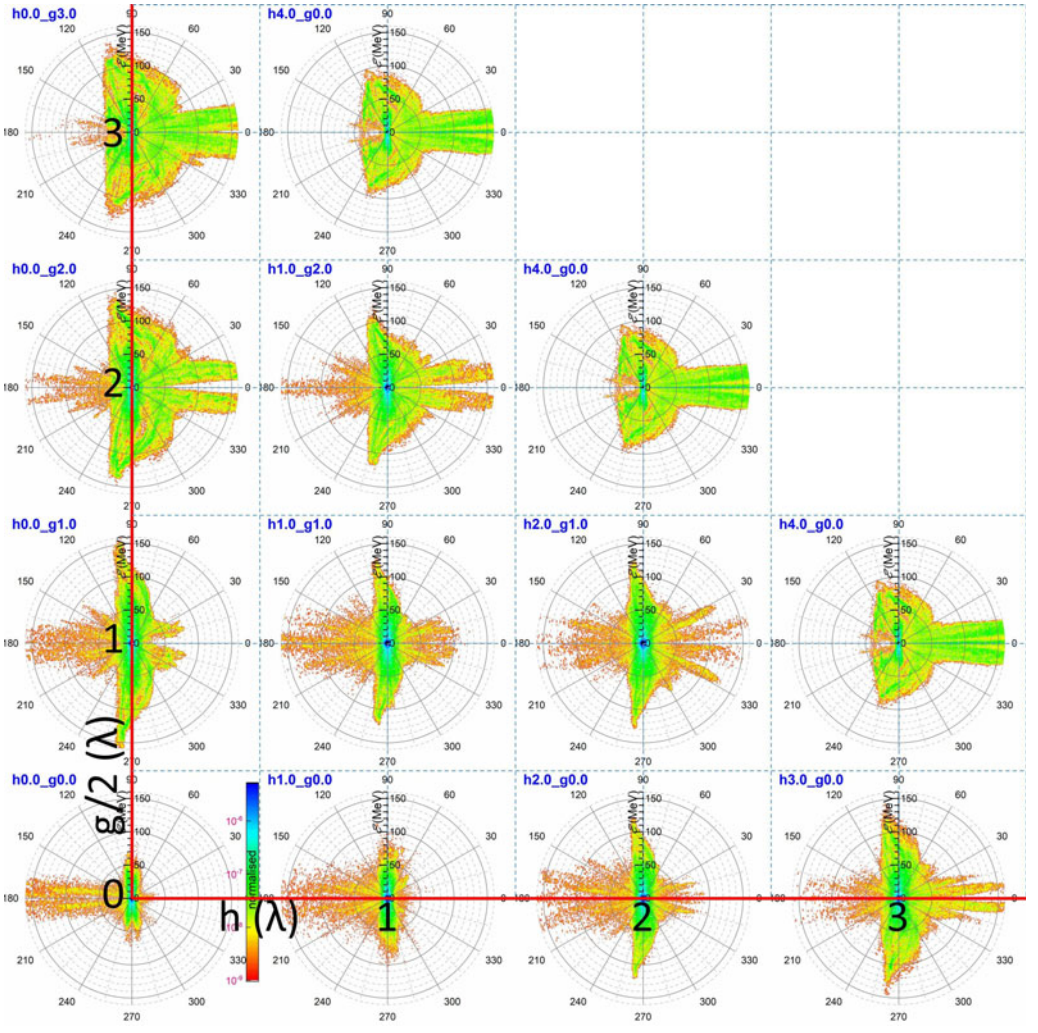


FIGURE 3. Electron energy polar diagrams for various combinations of the central-hole radius and the side-hole extent. The red lines form a Cartesian system where the holed-target characteristic dimensions (h and $g/2$) are given by the centre of each contour.

of MeV energies. Furthermore, the portion of the pulse captured by the foil drives electrons along the foil surface at an energy of ∼50 MeV.

The first column of figure 3 corresponds to HT1CH, where the hole extent is increasing towards the hypotenuse. As the hole extent increases, smaller amplitude fields are reflected, decreasing the energy and number of the target front electrons. On the other hand, the percentage of the diffracted pulse increases, preserving the initial shape of the pulse due to weaker diffraction by the increased hole. As a result, the target rear electrons are accelerated to hundreds of MeV energies. Notably, this behaviour has an optimum hole extent, since for an extremely large hole a drastic lowering of the pulse amplitude allows no electron ejection.

The last row of figure 3 corresponds to HT2SH, where the side-holes' extent is increasing towards the hypotenuse. Practically, by increasing the side-holes' extent

https://doi.org/10.1017/S0022377820000379 Published online by Cambridge University Press

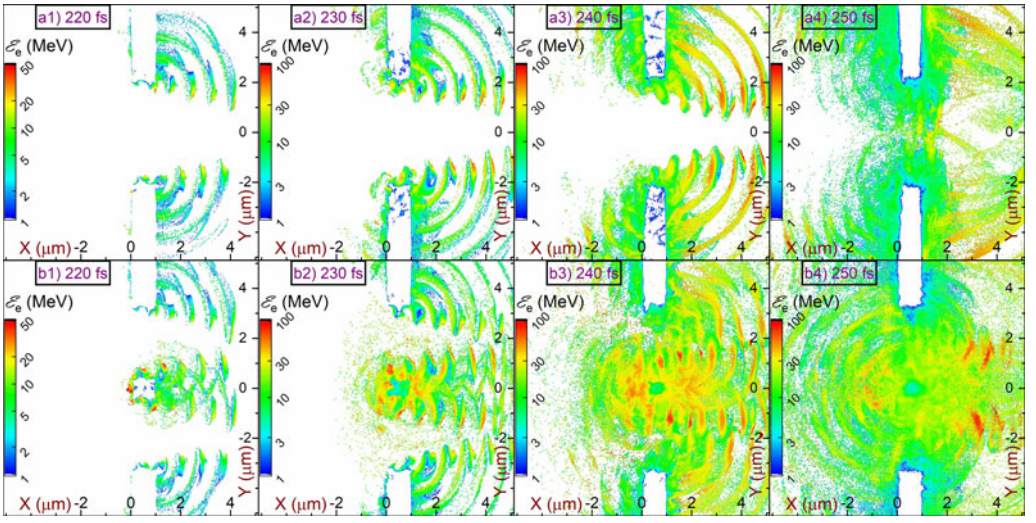


FIGURE 4. Evolution of the electron mean energy per cell corresponding to a ($a1$–$a4$) HT1CH with a central hole of 5λ and ($b1$–$b4$) HT2SH with two side holes of 3.5λ.

the inner-segment extent is decreased and, a smaller portion of the pulse is reflected by the inner segment. For small inner segments, electrons are preferably accelerated towards the target rear, but not as strongly as in the case of HT1CH. This is because the inner segment (located in the middle of the incident pulse) reflects the highest field amplitude but it also diffracts the remaining pulse, significantly attenuating it.

Ejection of hot electrons from the target leads to a charge imbalance, as seen in figure 5. The blue regions indicate an excess of negative charge, due to the capture of electrons by the laser field. However, the white (saturated) regions indicate an excess of protons and carbon ions, which eventually leads to CE. The positive core is stronger for a HT2SH with two side holes of $\sim 3.5\lambda$ since in that case most electrons are ejected from the inner segment at $\sim$230 fs, as can be realised by the large positively charged region in figure 5($c2$). The conditions under which CE dominates are given in equations (1) and (2) of Bulanov *et al.* (2016), which can be rearranged as

$$l < \frac{2\varepsilon_0 E}{e n_e}. \tag{3.2}$$

Here, l is the foil thickness, ε_0 is the permittivity of free space. E the electric field, e the elementary charge and n_e the electron number density. For a HT2SH with a central segment of λ, due to the 7λ total gap in the FWHM of the electric field, the target thickness should be 8 times larger since l in the equation above is volumetrically associated with the number of hot electrons. Therefore, for that specific case one should expect complete electron ejection at a central-segment thickness of $\sim$0.55 μm. However, due to the complex diffraction patterns the pulse is able to penetrate the central segment and extract electrons from both its front and rear surfaces, further relaxing the minimum target thickness required.

The percentage of the laser energy transferred to particles is also directly connected with the geometry of the holed target, as seen in figure 5($a1$). Although for a flat foil only $\sim$25 % of the energy is transferred to particles, this value approximately doubles

https://doi.org/10.1017/S0022377820000379 Published online by Cambridge University Press

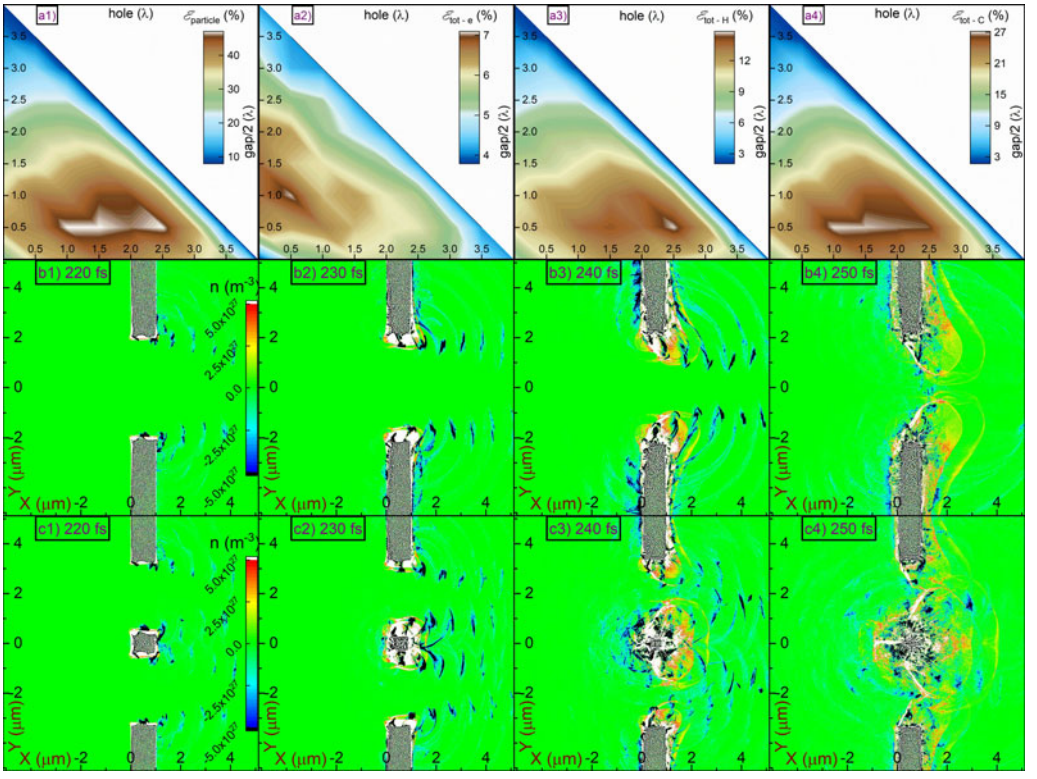


FIGURE 5. The percentage of laser energy transferred to (*a*1) all particles, (*a*2) electrons, (*a*3) protons and (*a*4) carbon ions by the end of the simulation. Evolution of the charge density per cell for a (*b*1–*b*4) HT1CH with a central hole of 5λ and (*c*1–*c*4) HT2SH with two side holes of 3.5λ.

for a holed target with a central hole of 0.5λ and side holes of 1–2.5λ. The drop of the conversion efficiency for larger holes is because, in this case, less particles interact with the laser pulse. Furthermore, the conversion efficiency for each particle species is maximised for different holed targets. For electrons (see figure 5*a*2), a clear peak is formed for a central hole of 1λ and side-holes of 0.5λ, while for protons (see figure 5*a*3) this value shifts to 0.5λ for the central hole and 2.5λ for the side holes. As for carbon ions (see figure 5*a*4), since they define most of the energy absorbed by particles, their optimum absorption corresponds to the same hole values as those of the total system, but with a slight optimisation for side holes of 1λ.

3.3. *Ion energy evolution and polar distribution*

A direct consequence of electron ejection from the target is acceleration of protons and carbon ions and a brief report on the main laser driven ion acceleration mechanisms is made in § 1.1. As described in § 1.2, the general holed-target geometry corresponds to two limiting cases (HT1CH and HT2SH), where a flat foil is the common geometry of these limits. Therefore, the holed-target geometry does not follow a single acceleration mechanism, and for different target parameters different acceleration mechanisms dominate.

https://doi.org/10.1017/S0022377820000379 Published online by Cambridge University Press

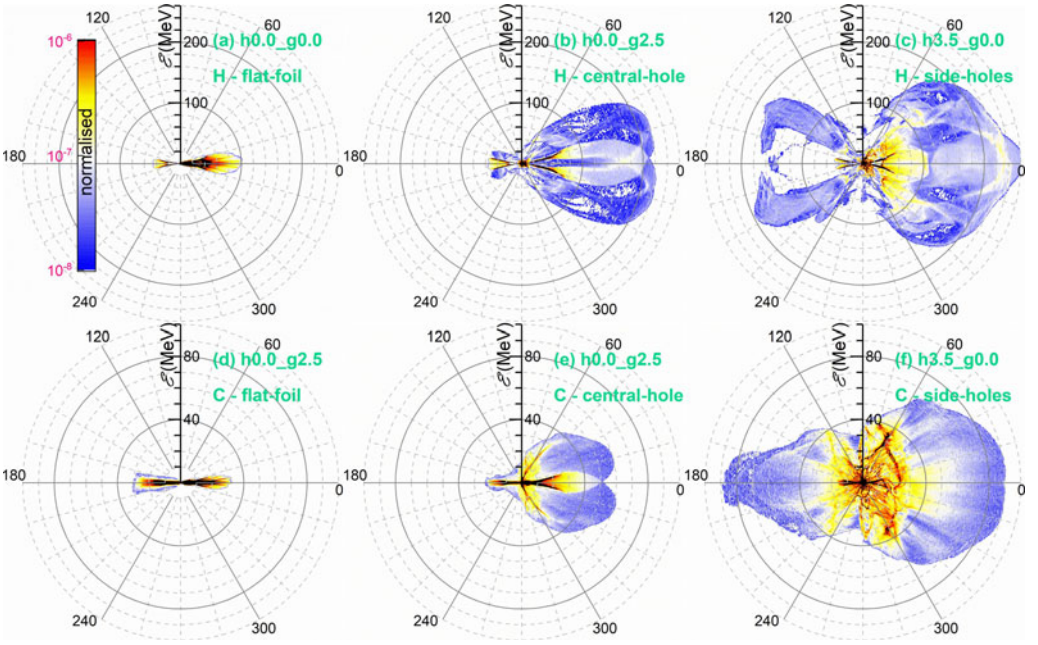


FIGURE 6. Proton energy polar diagrams corresponding to a (*a*) flat foil, (*b*) HT1CH with a central hole of 5λ and (*c*) HT2SH with two side holes of 3.5λ. Carbon ion energy polar diagrams corresponding to a (*d*) flat foil, (*e*) HT1CH with a central hole of 5λ and (*f*) a HT2SH with two side holes of 3.5λ.

In the unique case of the flat foil, the proton acceleration is due to the TNSA mechanism. In our case the target is a 1 μm polyethylene foil and the pulse is P-polarised, excluding any contribution of the RPA mechanism at the present intensity. Furthermore, the solid foil density does not allow the MVA mechanism to develop. Therefore, the simulations for a flat foil give only ∼100 MeV protons and ∼30 MeV per nucleon carbon ions, as shown in figure 6. The divergence of the beam is ∼30° full angle, as expected from the TNSA mechanism (Macchi *et al.* 2013).

Let us first consider the geometrically simplest limiting case, of a HT1CH. To understand how protons are accelerated from this configuration, one must consider the proton and carbon ion mean energy evolution, shown in figures 7(*b*) and 7(*c*), respectively, along with the evolution of the field components, shown in figure 2(*a*). Initially, the edges of the Gaussian pulse interact with the outer segments resulting in electron ejection. Therefore, a sheath field is created at the outer segments (practically they are two independent foils) weakly accelerating protons by a TNSA-like mechanism; since the acceleration is normal on the foil surfaces (both target rear and inner), protons originate from the target corners, as shown in figure 7(*b*2,*c*2). Furthermore, electron ejection leads to accumulation of a localised net positive charge (weak CE), as seen in figure 4(*b*2). As a result, protons reach the target rear region, as seen in figure 7(*b*3,*c*3). There, diffraction of the laser pulse leads to development of a longitudinal electric field (see figure 2*a*7–*a*12) which then accelerates the protons, as seen in figure 7(*b*4,*c*4). Since the diffracted longitudinal electric field exists only in the target rear region, protons in the target front region are only weakly accelerated due to the initial weak CE acceleration. The simulations show that although protons

https://doi.org/10.1017/S0022377820000379 Published online by Cambridge University Press

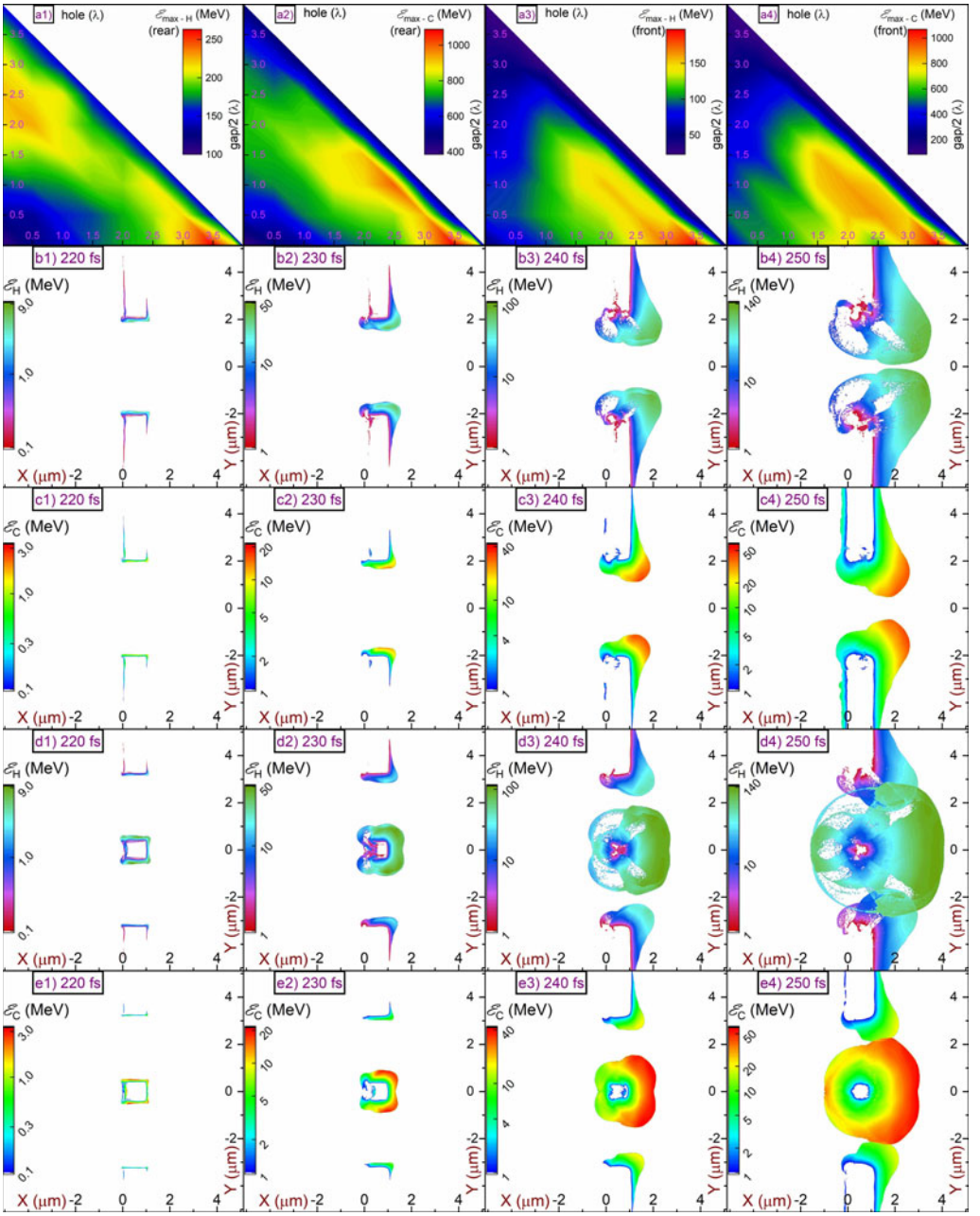


FIGURE 7. The maximum energy of holed-target (*a*1) rear protons, (*a*2) front protons, (*a*3) rear carbon ions and (*a*4) front carbon ions, by the end of the simulation. Evolution of the mean kinetic energy per cell for (*b*1–*b*4) protons and (*c*1–*c*4) carbon ions, for a HT1CH with a central hole of 5λ. Evolution of the mean kinetic energy per cell for (*d*1–*d*4) protons and (*e*1–*e*4) carbon ions, for a HT2SH with two side holes of 3.5λ.

are emitted with a divergence of $\sim$90° full angle, the vast majority are confined within $\sim$30°, as shown in figure 6(*b*).

https://doi.org/10.1017/S0022377820000379 Published online by Cambridge University Press

The acceleration mechanism governing the second holed-target limiting case, of HT2SH, is the well-examined CE mechanism, where the expected maximum proton energy is given by $\mathcal{E}_p \approx 173\sqrt{\mathcal{P}[\mathrm{PW}]}$ MeV ($\mathcal{P}[\mathrm{PW}]$ is the laser power in PW) (Bulanov *et al.* 2004, 2014) and for the present intensity corresponds to ∼180 MeV. The strong charge imbalance observed in figure 5(*c*3) indicates that the CE regime has been reached. Another indication of the CE mechanism is the similar energies of both the target front and target rear protons, as shown in figure 6(*c*); the same applies for carbon ions, seen in figure 6(*f*). Again, although protons have an overall divergence of ∼90°, an increased proton number is observed within a ∼30° full angle. The simulations suggest a maximum proton energy of ∼260 MeV, or ∼30 % higher, than what predicted in Bulanov *et al.* (2014). However, the holed targets do not obey a single acceleration mechanism, and additional acceleration due to the diffracted longitudinal electric field component (although not the dominant mechanism) must be acknowledged, as in the HT1CH case. Notably, if the inner segment is large enough to reflect most of the laser pulse, then electrons are not effectively ejected and the inner segment does not undergo strong CE. In that case, the situation resembles an intermediate regime of CE and TNSA, where the TNSA dominates for larger inner segments. Therefore, by increasing the inner-segment extent, the maximum proton energy is reduced, approaching the energy obtained from a flat foil.

The results for the many geometrical combinations of the holed targets are visually represented in figure 7(*a*1–*a*4), where the maximum proton and carbon ion energy is plotted as a function of the side-hole and central-hole dimensions, for both the target front and rear surfaces. From figure 7(*a*1) it is observed that two local maxima exist at the contour of the rear surface proton energy (figure 7*a*1), corresponding to the transition of the general holed-target geometry to the two limiting cases. The highest energy maximum corresponds to the HT2SH. Since in that geometry CE dominates, an energy maximum exists for the same geometric configuration (same contour location) in figure 7(*a*3) corresponding to the target front protons, but also in figures 7(*a*2) and 7(*a*4) corresponding to carbon ions. The extent of the inner segment suggests an optimum proton energy value, where all electrons are ejected from the inner segment, leaving an ion core. However, if the inner segment is further reduced, the ion core becomes smaller, resulting in a weaker CE. On the other hand, for the case of a HT1CH, the energy maximum is observed only in figure 7(*a*1) due to the absence of the longitudinal electric field in the target front region; the energy maximum is weaker in figure 7(*a*2) due to the lower charge to mass ratio of carbon ions compared to protons.

3.4. *Electron and ion spectra from holed targets*

The qualitative results of figure 7(*a*1–*a*4) are quantified in figures 8 and 9, where spectra for electrons, protons and carbon ions are extracted for both limiting holed-target geometries. The spectra from the 2-D simulations have been rescaled to the equivalent 3-D spectra (Hadjisolomou *et al.* 2020) assuming a 4.75 μm emission region diameter.

The energy gain of several hot electron populations is explained in § 3.2 and pictured in figure 3. However, the target rear electron spectra from holed targets reveal a significantly enhanced flux compared to flat foils (black line in figures 8 and 9); notably, the opposite behaviour occurs for target front electrons. The flat-foil simulations suggest a hot electron temperature of ∼5.5 MeV; for the intensity used,

https://doi.org/10.1017/S0022377820000379 Published online by Cambridge University Press

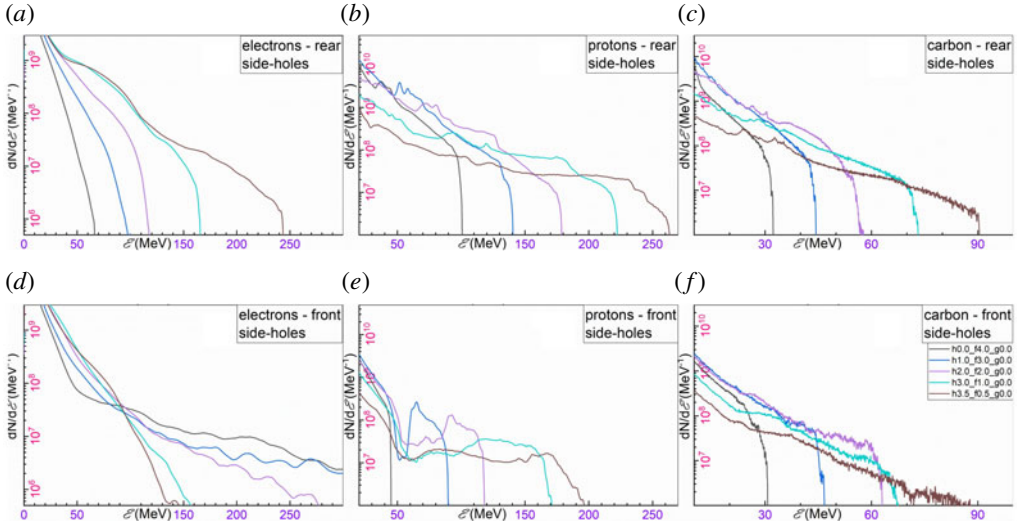


FIGURE 8. Energy spectra of (*a*) electrons, (*b*) protons and (*c*) carbon ions corresponding to the rear of a HT2SH. Energy spectra of (*d*) electrons, (*e*) protons and (*f*) carbon ions corresponding to the front of a HT2SH. The target geometry is defined by the *g* and *h* parameters as labelled in (*f*), while the black line corresponds to a flat foil.

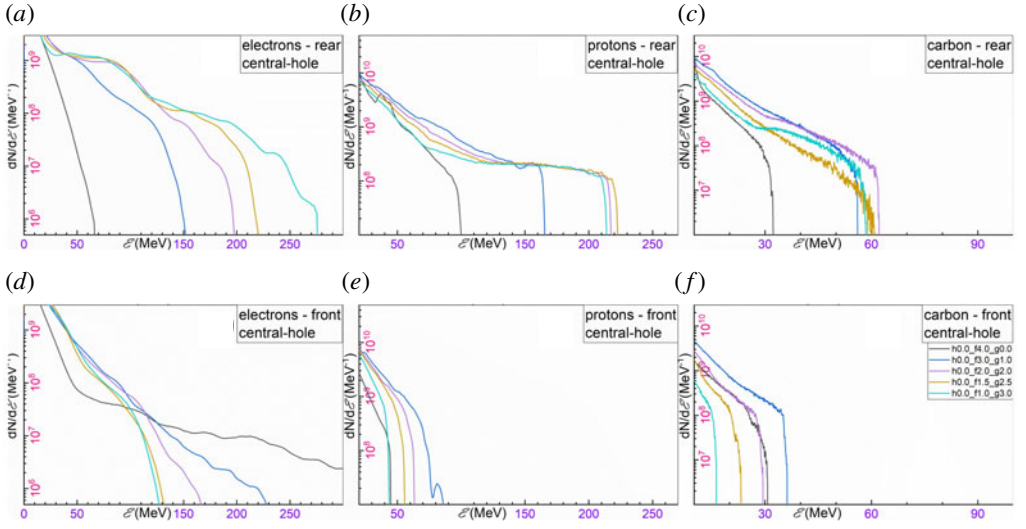


FIGURE 9. Energy spectra of (*a*) electrons, (*b*) protons and (*c*) carbon ions corresponding to the rear of a HT1CH. Energy spectra of (*d*) electrons, (*e*) protons and (*f*) carbon ions corresponding to the front of a HT1CH. The target geometry is defined by the *g* and *h* parameters as labelled in (*f*), while the black line corresponds to a flat foil.

Haines scaling (Haines *et al.* 2009) gives ∼4 MeV and Kluge scaling (Kluge *et al.* 2011) gives ∼7 MeV. On the other hand, the holed-target geometry suggests an electron temperature of ∼30 MeV for HT2SH and ∼40 MeV for HT1CH (brown lines in figures 8(*a*) and 9(*a*) respectively).

https://doi.org/10.1017/S0022377820000379 Published online by Cambridge University Press

The target rear proton spectra for a HT2SH is shown in figure 8(*b*). Although the cutoff proton energy is also shown in figure 7(*a*), the spectra reveal the reduction of the total number of accelerated protons for increased maximum proton energy due to shrinkage of the inner segment from which the high energy protons originate. Despite the proton number reduction, a continuously increasing temperature is observed for increasing maximum proton energy (see figure 8*b*). Therefore, the envelope of all cases of maximum proton energy appears with an exponential-like decaying behaviour. A similar trend is also seen for carbon ions, as shown in figure 8(*c*).

On the other hand, the target rear proton spectra for HT1CH exhibit several qualitative differences. The maximum proton energy follows an increasing trend with increasing the central-hole extent, up to $\sim 2\lambda$. Then, for an increasing central hole up to $\sim 3\lambda$ the maximum proton energy remains practically unchanged, with a maximum at $\sim 2.5\lambda$. Following that maximum region, further increase in the central-hole extent drastically reduces the maximum proton energy. Regardless of the target geometry, all spectra are characterised by a double exponential decaying function and a sharp cutoff energy (see figure 9*b*). Notably, the volumetric reduction of the number of accelerated protons is not obvious, since the accelerated protons originate from the perimeter of the central hole. For a large central hole, although a larger perimeter suggests a larger number of protons available for acceleration, a weaker combination of TNSA and CE drives less protons into the region of the accelerating component of the diffracted electric field.

3.5. *Towards mass-limited targets*

Although the concept of ML targets is very attractive due to promising simulation results on enhancement of the maximum proton energy (Limpouch *et al.* 2008; Bulanov *et al.* 2010*a*; Kluge *et al.* 2010; Lezhnin *et al.* 2016), an experimental verification and implementation of the method is challenging (Sokollik *et al.* 2010; Paasch-Colberg *et al.* 2011). However, a ML foil is the limit of a HT2SH, when the extent of the side holes tends to infinity. A summary of the simulation results is shown in figure 10, where the inner segment has 1λ extent.

At the other side of the limit, where the side holes have a zero extent, the target corresponds to a flat foil. There, the target rear protons have an energy of $\sim$100 MeV. However, the addition of two side holes of $\sim 2\lambda$ doubles the initial energy, while expansion of the side holes to infinity approximately triples the energy. Similar observations occur for the target front protons, where a flat-foil energy of $\sim$50 MeV becomes four times higher when the side holes tend to infinity. The same qualitative results also apply for carbon ions, where the initial $\sim$35 MeV per nucleon are tripled, for both the target front and rear. In conclusion, the concept of a ML target gives approximately the same maximum proton energy with a HT2SH with sufficiently large side holes, of $\sim 5\lambda$ extent.

As mentioned for figure 5, the holed-target geometry significantly increases the transfer of laser energy into particles. This effect can also be seen by the black lines in figure 10, where the dashed, dashed-dotted and dotted lines correspond to the percentage of the laser energy transferred to electrons, protons and carbon ions respectively; notably, the trend for all three particles is very similar regardless the value of the side holes. For the case of a flat foil, the overall particle energy is $\sim 25\,\%$, while the addition of two side holes of $\sim 1\lambda$ approximately doubles the absorbed energy. However, further increase of the side-holes' dimensions lowers the laser energy transformation since a larger portion of the pulse does not interact

https://doi.org/10.1017/S0022377820000379 Published online by Cambridge University Press

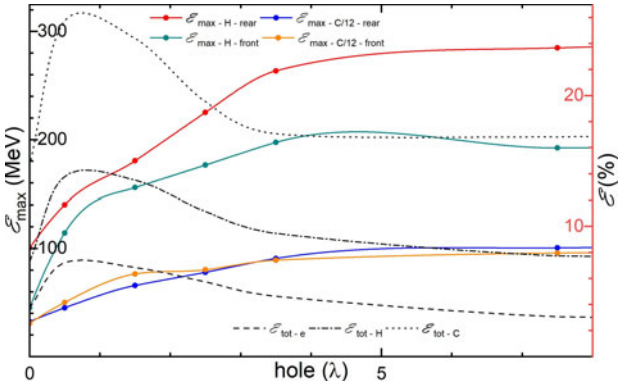


FIGURE 10. The target corresponds to a generalisation of the HT2SH. By increasing the side-holes' extent and keeping the inner segment constant, the target transits from a flat-foil to a ML target. (Left) The maximum proton and carbon ion energy per nucleon for both the target rear and front, as indicated by the labels in the figure. (Right) The percentage of the laser energy transferred to electrons, protons and carbon ions is indicated by the dash, dash-dot and dot line respectively.

with the target. By increasing the side holes to $\sim 3.5\lambda$ (equivalent to two standard deviations of the electric field) then only $\sim 5\,\%$ of the pulse interacts with the outer segments and the contribution of the pulse can be ignored. At that point, the laser energy transformation is solely due to the inner segment, saturating at an energy conversion efficiency of $\sim 28\,\%$. Therefore, one must compromise between the highest proton energy obtained from ML targets and the maximum laser energy conversion efficiency obtained from HT2SH with holes of $\sim 1\lambda$.

4. Summary and conclusions

Microstructured targets have gained significant popularity in laser-driven particle acceleration with many target designs already proposed. In the present work an innovative target geometry is introduced, where three holes are created on a flat foil. This general holed-target geometry has two limits, where at the first limit the inner segments can be joined together, leaving only two side holes in the target and is named HT2SH. At the second limit, the inner segments are joined to the outer segments, leaving only a central hole on the foil, named HT1CH. The length sum of the three holes plus the inner segments is constant at 8λ, corresponding to the electric field FWHM of the laser pulse. By plotting the contour of the side holes and the central-hole extent, all geometrical combinations of the holed targets are represented in an orthogonal triangular area, where the orthogonal angle of the triangle corresponds to a flat foil which is the common geometry of the two limit groups.

The contour plots for the laser energy transformed into particle energy reveal that the holed-target geometry significantly enhances the laser energy conversion efficiency, where for some cases the improvement is approximately double compared to flat foils. The different particles constituting the polyethylene target used do not have optimum conversion efficiency for the same holed-target geometry; electrons have an optimum at a $\sim 1\lambda$ central hole and $\sim 0.5\lambda$ side holes, while protons at $\sim 0.5\lambda$ central hole and $\sim 2.5\lambda$ side holes.

https://doi.org/10.1017/S0022377820000379 Published online by Cambridge University Press

The holed targets take advantage of the laser pulse reflection, diffraction and interference to manipulate the electron energy spectra and their spatial distribution. If a hot electron population is captured by the laser pulse then it is continuously accelerated until it is dephased. In the case of a flat foil, most of the pulse is reflected by the foil front surface and the captured electrons are accelerated in a direction opposite to the laser pulse. On the other hand, the holed-target geometry diffracts the pulse on the target rear region, where the electrons are now favourably accelerated. In addition, the electron temperature is significantly enhanced by holed targets. However, this optimised behaviour ceases if the holes become extremely large, because the pulse edges do not sufficiently generate hot electrons at the initial stages of the interaction.

The maximum proton energy contour plots for the target rear create a pattern where two local maxima are observed. These two maxima correspond to the two limiting cases of the general holed-target geometry, where the highest is for the HT2SH. The dominant acceleration mechanism on that limit is the CE acceleration, where by reducing the dimensions of the inner segment to an optimum value, protons of $\sim$260 MeV are emitted. This value is higher than the $\sim$180 MeV predicted for CE, indicating that the acceleration is slightly enhanced by a secondary mechanism. This secondary mechanism is the main acceleration mechanism for HT1SH. There, due to diffraction of the laser pulse, a longitudinal electric field is created which is responsible for the $\sim$220 MeV proton energy observed. In contrast with CE, only low energy target front protons are emitted.

If the length sum of the side holes and the inner segments is not constant then another limiting case is considered by generalisation of the HT2SH (which is a sub-case itself), which is the transition from a flat foil to a ML target. This transition occurs by keeping the central foil constant and gradually increasing the extent of the side holes. It is found that the energy absorption is optimised for side holes of $\sim 1\lambda$ and it rapidly drops as the transition to ML targets occurs, due to less available particles in the laser focal spot. On the other hand, the maximum proton energy is significantly increased for increased side-holes' extent, where a near-maximum value is obtained for side holes of $\sim 4\lambda$, indicating that the ML targets have almost no benefit in particle acceleration compared to holed targets. Therefore, a compromise must be made regarding optimisation of both conversion efficiency and maximum proton energy.

Acknowledgements

The authors acknowledge fruitful discussions with P. Sasorov and T. M. Jeong, and thank A. Molodozhentsev for providing a significant part of the computational resources used. This work is supported by the project High Field Initiative (CZ.02.1.01/0.0/0.0/15_003/0000449) from the European Regional Development Fund. It was also in part funded by the UK EPSRC grants EP/G054950/1, EP/G056803/1, EP/G055165/1 and EP/M022463/1.

REFERENCES

ARBER, T. D., BENNETT, K., BRADY, C. S., LAWRENCE-DOUGLAS, A., RAMSAY, M. G., SIRCOMBE, N. J., GILLIES, P., EVANS, R. G., SCHMITZ, H., BELL, A. R. *et al.* 2015 Contemporary particle-in-cell approach to laser-plasma modelling. *Plasma Phys. Control. Fusion* **57** (11), 1–26.

ATZENI, S., TEMPORAL, M. & HONRUBIA, J. J. 2002 A first analysis of fast ignition of precompressed ICF fuel by laser-accelerated protons. *Nucl. Fusion* **42** (3), 1–4.

https://doi.org/10.1017/S0022377820000379 Published online by Cambridge University Press

BAMBERGER, E. & TSCHIRNER, F. 1900 Ueber die Einwirkung von Diazomethan auf β-Arylhydroxylamine. *Ber. Dtsch. Chem. Ges.* **33**, 955–959.

BARGSTEN, C., HOLLINGER, R., CAPELUTO, M., KAYMAK, V., PUKHOV, A., WANG, S., ROCKWOOD, A., WANG, Y., KEISS, D., TOMMASINI, R. *et al.* 2017 Energy penetration into arrays of aligned nanowires irradiated with relativistic intensities: scaling to terabar pressures. *Sci. Adv.* **3**, e1601558.

BARTAL, T., FOORD, M. E., BELLEI, C., KEY, M. H., GAILLARD, K. A., FLIPPO, S. A., OFFERMANN, D. T., PATEL, P. K., JARROTT, L. C., HIGGINSON, D. P. *et al.* 2012 Focusing of short-pulse high-intensity laser-accelerated proton beams. *Nat. Phys.* **8**, 139–142.

BASHINOV, A. V., GONOSKOV, A. A., KIM, A. V., MOUROU, G. & SERGEEV, A. M. 2014 New horizons for extreme light physics with mega-science project XCELS. *Eur. Phys. J. Spec. Top.* **223** (6), 1105–1112.

BOODY, F. P., HÖPFL, R., HORA, H. & KELLY, J. C. 1996 Laser-driven ion source for reduced-cost implantation of metal ions for strong reduction of dry friction and increased durability. *Laser Part. Beams* **14** (3), 443–448.

BORGHESI, M., CAMPBELL, D. H., SCHIAVI, A., HAINES, M. G., WILLI, O., MACKINNON, A. J., PATEL, P., GIZZI, L. A., GALIMBERTI, M., CLARKE, R. J. *et al.* 2002 Electric field detection in laser–plasma interaction experiments via the proton imaging technique. *Phys. Plasmas* **9** (5), 2214–2220.

BORGHESI, M., ROMAGNANI, L., SCHIAVI, A., CAMPBELL, D. H., HAINES, M. G., WILLI, O., MACKINNON, A. J., GALIMBERTI, M., GIZZI, L., CLARKE, R. J. *et al.* 2003 Measurement of highly transient electrical charging following high-intensity lasersolid interaction. *Appl. Phys. Lett.* **82** (10), 1529–1531.

BORIS, J. P. 1970 Relativistic plasma simulation-optimization of a hybrid code. In *Proceeding of Fourth Conference on Numerical Simulations of Plasmas*, pp. 3–67. Naval Research Laboratory, Washington, D.C.

BORN, M. & WOLFL, E. 1999 *Principles of Optics: Electromagnetic Theory of Propagation, Interference and Diffraction of Light*, 7th edn. Cambridge University Press.

BRAENZEL, J., ANDREEV, A. A., ABICHT, F., EHRENTRAUT, L., PLATONOV, K. & SCHNÜRER, M. 2017 Amplification of relativistic electron bunches by acceleration in laser fields. *Phys. Rev. Lett.* **118**, 014801.

BULANOV, S. S., BRANTOV, A., BYCHENKOV, V. Y., CHVYKOV, V., KALINCHENKO, G., MATSUOKA, T., ROUSSEAU, P., REED, S., YANOVSKY, V., LITZENBERG, D. W. *et al.* 2008 Accelerating monoenergetic protons from ultrathin foils by flat-top laser pulses in the directed-Coulomb-explosion regime. *Phys. Rev.* E **78**, 026412.

BULANOV, S. S., ESAREY, E., SCHROEDER, C. B., BULANOV, S. V., ESIRKEPOV, T. Z., KANDO, M., PEGORARO, F. & LEEMANS, W. P. 2016 Radiation pressure acceleration: the factors limiting maximum attainable ion energy. *Phys. Plasmas* **23** (5), 056703.

BULANOV, S. S., BYCHENKOV, V. Y., CHVYKOV, V., KALINCHENKO, G., LITZENBERG, D. W., MATSUOKA, T., THOMAS, A. G. R., WILLINGALE, L., YANOVSKY, V., KRUSHELNICK, K. *et al.* 2010*b* Generation of GeV protons from 1 PW laser interaction with near critical density targets. *Phys. Plasmas* **17** (4), 043105.

BULANOV, S. V., DAIDO, H., ESIRKEPOV, T. Z., KHOROSHKOV, V. S., KOGA, J., NISHIHARA, K., PEGORARO, F., TAJIMA, T. & YAMAGIWA, M. 2004 Feasibility of using laser ion accelerators in proton therapy. *AIP Conf. Proc.* **740** (1), 414–429.

BULANOV, S. V. & ESIRKEPOV, T. Z. 2007 Comment on 'Collimated Multi-MeV Ion Beams from High-Intensity Laser Interactions with Underdense Plasma'. *Phys. Rev. Lett.* **98**, 049503.

BULANOV, S. V., ESIRKEPOV, T. Z., CALIFANO, F., KATO, Y., LISEIKINA, T. V., MIMA, K., NAUMOVA, N. M., NISHIHARA, K., PEGORARO, F., RUHL, H. *et al.* 2000 Generation of collimated beams of relativistic ions in laser-plasma interactions. *J. Expl Theor. Phys. Lett.* **71** (10), 407–411.

BULANOV, S. V., ESIRKEPOV, T. Z., KAMENETS, F. F., KATO, Y., KUZNETSOV, A. V., NISHIHARA, K., PEGORARO, F., TAJIMA, T. & KHOROSHKOV, V. S. 2002 Generation of high-quality

https://doi.org/10.1017/S0022377820000379 Published online by Cambridge University Press

charged particle beams during the acceleration of ions by high-power laser radiation. *Plasma Phys. Rep.* **28**, 975–991.

BULANOV, S. V. & KHOROSHKOV, V. S. 2002 Feasibility of using laser ion accelerators in proton therapy. *Plasma Phys. Rep.* **28** (5), 453–456.

BULANOV, S. S., LITZENBERG, D. W., KRUSHELNICK, K. & MAKSIMCHUK, A. 2010*a* Directed Coulomb Explosion regime of ion acceleration from mass limited targets by linearly and circularly polarized laser pulses. arXiv:1007.3963.

BULANOV, S. V., WILKENS, J. J., ESIRKEPOV, T. Z., KORN, G., KRAFT, G., KRAFT, S. D., MOLLS, M. & KHOROSHKOV, V. S. 2014 Laser ion acceleration for hadron therapy. *Phys.-Uspekhi* **57** (12), 1149–1179.

BULANOV, S. V., YOGO, A., ESIRKEPOV, T. Z., KOGA, J. K., BULANOV, S. S., KONDO, K. & KANDO, M. 2015 Stochastic regimes in the driven oscillator with a step-like nonlinearity. *Phys. Plasmas* **22** (6), 063108.

BURZA, M., GONOSKOV, A., GENOUD, G., PERSSON, A., SVENSSON, K., QUINN, M., MCKENNA, P., MARKLUND, M. & WAHLSTRÖM, C. G. 2011 Hollow microspheres as targets for staged laser-driven proton acceleration. *New J. Phys.* **13** (1), 013030.

DAIDO, H., NISHIUCHI, M. & PIROZHKOV, A. S. 2012 Review of laser-driven ion sources and their applications. *Rep. Prog. Phys.* **75** (5), 056401.

DITMIRE, T., TISCH, J. W. G., SPRINGATE, E., MASON, M. B., HAY, N., SMITH, R. A., MARANGOS, J. & HUTCHINSON, M. H. R. 1997 High-energy ions produced in explosions of superheated atomic clusters. *Nature* **386**, 54–56.

ESIRKEPOV, T. Z., BORGHESI, M., BULANOV, S. V., MOUROU, G. & TAJIMA, T. 2004 Highly efficient relativistic-ion generation in the laser-piston regime. *Phys. Rev. Lett.* **92**, 175003.

ESIRKEPOV, T. Z., BULANOV, S. V., NISHIHARA, K., TAJIMA, T., PEGORARO, F., KHOROSHKOV, V. S., MIMA, K., DAIDO, H., KATO, Y., KITAGAWA, Y. *et al.* 2002 Proposed double-layer target for the generation of high-quality laser-accelerated ion beams. *Phys. Rev. Lett.* **89**, 175003.

FISCHER, J. & WEGENER, M. 2013 Three-dimensional optical laser lithography beyond the diffraction limit. *Laser Photonics Rev.* **7** (1), 22–44.

HADJISOLOMOU, P., TSYGVINTSEV, I. P., SASOROV, P., GASILOV, V., KORN, G. & BULANOV, S. V. 2020 Preplasma effects on laser ion generation from thin foil targets. *Phys. Plasmas* **27** (1), 013107.

HAINES, M. G., WEI, M. S., BEG, F. N. & STEPHENS, R. B. 2009 Hot-electron temperature and laser-light absorption in fast ignition. *Phys. Rev. Lett.* **102**, 045008.

HIGGINSON, A., GRAY, R. J., KING, M., DANCE, R. J., WILLIAMSON, S. D. R., BUTLER, N. M. H., WILSON, R., CAPDESSUS, R., ARMSTRONG, C., GREEN, J. S. *et al.* 2018 Near-100 MeV protons via a laser-driven transparency-enhanced hybrid acceleration scheme. *Nat Commun.* **9** (724).

HIGUERA, A. V. & CARY, J. R. 2017 Structure-preserving second-order integration of relativistic charged particle trajectories in electromagnetic fields. *Phys. Plasmas* **24** (5), 052104.

JI, L. L., SNYDER, J., PUKHOV, A., FREEMAN, R. R. & AKLI, K. U. 2016 Towards manipulating relativistic laser pulses with micro-tube plasma lenses. *Sci. Rep.* **6**, 23256.

JI, L. L., SNYDER, J. & SHEN, B. F. 2019 Single-pulse laser-electron collision within a micro-channel plasma target. *Plasma Phys. Control. Fusion* **61** (6), 065019.

JIANG, S., JI, L. L., AUDESIRK, H., GEORGE, K. M., SNYDER, J., KRYGIER, A., POOLE, P., WILLIS, C., DASKALOVA, R., CHOWDHURY, E. *et al.* 2016 Microengineering laser plasma interactions at relativistic intensities. *Phys. Rev. Lett.* **116**, 085002.

KAWATA, S., NAGASHIMA, T., TAKANO, M., IZUMIYAMA, T., KAMIYAMA, D., BARADA, D., KONG, Q., GU, Y., WANG, P., MA, Y. Y. *et al.* 2014 Controllability of intense-laser ion acceleration. *High Power Laser Sci. Eng.* **2**, doi:10.1017/hpl.2014.5.

KIM, I. J., PAE, K. H., CHOI, I. W., LEE, C. L., KIM, H. T., SINGHAL, H., SUNG, J. H., LEE, S. K., LEE, H. W., NICKLES, P. V. *et al.* 2016 Radiation pressure acceleration of protons to 93 MeV with circularly polarized petawatt laser pulses. *Phys. Plasmas* **23** (7), 070701.

https://doi.org/10.1017/S0022377820000379 Published online by Cambridge University Press

KLIMO, O., PSIKAL, J., LIMPOUCH, J., PROSKA, J., NOVOTNY, F., CECCOTTI, T., FLOQUET, V. & KAWATA, S. 2011 Short pulse laser interaction with micro-structured targets: simulations of laser absorption and ion acceleration. *New J. Phys.* **13** (5), 053028.

KLIMO, O., PSIKAL, J., LIMPOUCH, J. & TIKHONCHUK, V. T. 2008 Monoenergetic ion beams from ultrathin foils irradiated by ultrahigh-contrast circularly polarized laser pulses. *Phys. Rev. ST Accel. Beams* **11**, 031301.

KLUGE, T., COWAN, T., DEBUS, A., SCHRAMM, U., ZEIL, K. & BUSSMANN, M. 2011 Electron temperature scaling in laser interaction with solids. *Phys. Rev. Lett.* **107**, 205003.

KLUGE, T., ENGHARDT, W., KRAFT, S. D., SCHRAMM, U., ZEIL, K., COWAN, T. E. & BUSSMANN, M. 2010 Enhanced laser ion acceleration from mass-limited foils. *Phys. Plasmas* **17** (12), 123103.

KURUP, A., PASTERNAK, J., TAYLOR, R., MURGATROYD, L., ETTLINGER, O., SHIELDS, W., NEVAY, L., GRUBER, S., POZIMSKI, J., LAU, H. T. *et al.* 2019 Simulation of a radiobiology facility for the Centre for the Clinical Application of Particles. *Phys. Med.* **65**, 21–28.

LEZHNIN, K. V., KAMENETS, F. F., ESIRKEPOV, T. Z., BULANOV, S. V., KLIMO, O., WEBER, S. & KORN, G. 2016 Laser ion acceleration from mass-limited targets with preplasma. *Phys. Plasmas* **23** (5), 053114.

LI, Y. T., YUAN, X. H., XU, M. H., ZHENG, Z. Y., SHENG, Z. M., CHEN, M., MA, Y. Y., LIANG, W. X., YU, Q. Z., ZHANG, Y. *et al.* 2006 Observation of a fast electron beam emitted along the surface of a target irradiated by intense femtosecond laser pulses. *Phys. Rev. Lett.* **96**, 165003.

LIMPOUCH, J., PSIKAL, J., ANDREEV, A. A., PLATONOV, K. Y. & KAWATA, S. 2008 Enhanced laser ion acceleration from mass-limited targets. *Laser Part. Beams* **26** (2), 225–234.

MACCHI, A., BORGHESI, M. & PASSONI, M. 2013 Ion acceleration by superintense laser-plasma interaction. *Rev. Mod. Phys.* **85**, 751–793.

MAKSIMCHUK, A., GU, S., FLIPPO, K., UMSTADTER, D. & BYCHENKOV, V. 2000 Forward ion acceleration in thin films driven by a high-intensity laser. *Phys. Rev. Lett.* **84**, 4108–4111.

MAO, J. Y., CHEN, L. M., GE, X. L., ZHANG, L., YAN, W. C., LI, D. Z., LIAO, G. Q., MA, J. L., HUANG, K., LI, Y. T. *et al.* 2012 Spectrally peaked electron beams produced via surface guiding and acceleration in femtosecond laser-solid interactions. *Phys. Rev.* E **85**, 025401.

MARGARONE, D., KLIMO, O., KIM, I. J., PROKŮPEK, J., LIMPOUCH, J., JEONG, T. M., MOCEK, T., PŠIKAL, J., KIM, H. T., PROŠKA, J. *et al.* 2012 Laser-driven proton acceleration enhancement by nanostructured foils. *Phys. Rev. Lett.* **109**, 234801.

MORITA, T., ESIRKEPOV, T. Z., BULANOV, S. V., KOGA, J. & YAMAGIWA, M. 2008 Tunable high-energy ion source via oblique laser pulse incident on a double-layer target. *Phys. Rev. Lett.* **100**, 145001.

MOUROU, G. A., TAJIMA, T. & BULANOV, S. V. 2006 Optics in the relativistic regime. *Rev. Mod. Phys.* **78**, 309–371.

MURAKAMI, M., HISHIKAWA, Y., MIYAJIMA, S., OKAZAKI, Y., SUTHERLAND, K., ABE, M., BULANOV, S. V., DAIDO, H., ESIRKEPOV, T. Z., KOGA, J. *et al.* 2008 Radiotherapy using a laser proton accelerator. *AIP Conf. Proc.* **1024**, 275–300.

NAGASHIMA, T., TAKANO, M., IZUMIYAMA, T., BARADA, D., KAWATA, S., GU, Y., KONG, Q., WANG, P., MA, Y. Y. & WANG, W. M. 2013 High-quality ion beam generation in laser plasma interaction. In *Proceedings of the 12th Asia Pacific Physics Conference (APPC12)*; doi:10.7566/JPSCP.1.015093.

NAKAJIMA, H., TOKITA, S., INOUE, S., HASHIDA, M. & SAKABE, S. 2013 Divergence-free transport of laser-produced fast electrons along a meter-long wire target. *Phys. Rev. Lett.* **110**, 155001.

OGURA, K., NISHIUCHI, M., PIROZHKOV, A. S., TANIMOTO, T., SAGISAKA, A., ESIRKEPOV, T. Z., KANDO, M., SHIZUMA, T., HAYAKAWA, T., KIRIYAMA, H. *et al.* 2012 Proton acceleration to 40 MeV using a high intensity, high contrast optical parametric chirped-pulse amplification/Ti:sapphire hybrid laser system. *Opt. Lett.* **37** (14), 2868–2870.

PAASCH-COLBERG, T., SOKOLLIK, T., GORLING, K., EICHMANN, U., STEINKE, S., SCHNÜRER, M., NICKLES, P. V., ANDREEV, A. & SANDNER, W. 2011 New method for laser driven ion

https://doi.org/10.1017/S0022377820000379 Published online by Cambridge University Press

acceleration with isolated, mass-limited targets. *Nucl. Instrum. Methods Phys. Res.* A **653** (1), 30–34.

PARK, J., BULANOV, S. S., BIN, J., JI, Q., STEINKE, S., VAY, J. L., GEDDES, C. G. R., SCHROEDER, C. B., LEEMANS, W. P., SCHENKEL, T. *et al.* 2019 Ion acceleration in laser generated megatesla magnetic vortex. *Phys. Plasmas* **26** (10), 103108.

PASSONI, M., BERTAGNA, L. & ZANI, A. 2010 Target normal sheath acceleration: theory, comparison with experiments and future perspectives. *New J. Phys.* **12** (4), 045012.

PATEL, P. K., MACKINNON, A. J., KEY, M. H., COWAN, T. E., FOORD, M. E., ALLEN, M., PRICE, D. F., RUHL, H., SPRINGER, P. T. & STEPHENS, R. 2003 Isochoric heating of solid-density matter with an ultrafast proton beam. *Phys. Rev. Lett.* **91**, 125004.

QIAO, B., FOORD, M. E., WEI, M. S., STEPHENS, R. B., KEY, M. H., MCLEAN, H., PATEL, P. K. & BEG, F. N. 2013 Dynamics of high-energy proton beam acceleration and focusing from hemisphere-cone targets by high-intensity lasers. *Phys. Rev.* E **87**, 013108.

QUINN, K., WILSON, P. A., CECCHETTI, C. A., RAMAKRISHNA, B., ROMAGNANI, L., SARRI, G., LANCIA, L., FUCHS, J., PIPAHL, A., TONCIAN, T. *et al.* 2009 Laser-driven ultrafast field propagation on solid surfaces. *Phys. Rev. Lett.* **102**, 194801.

RIPPERDA, B., BACCHINI, F., TEUNISSEN, J., XIA, C., PORTH, O., SIRONI, L., LAPENTA, G. & KEPPENS, R. 2018 A comprehensive comparison of relativistic particle integrators. *Astrophys. J.* **235** (1), 21.

ROBINSON, A. P. L., ZEPF, M., KAR, S., EVANS, R. G. & BELLEI, C. 2008 Radiation pressure acceleration of thin foils with circularly polarized laser pulses. *New J. Phys.* **10** (1), 013021.

ROCCA, J. J., SHLYAPTSEV, V., HOLLINGER, R., BARGSTEN, C., PUKHOV, A., KAYMAK, V., TOMMASINI, R., LONDON, R., PARK, J. & CAPELUTO, M. 2017 Compact ultra-intense lasers and nanostructures open a path to extreme pressures. *Laser Focus World* **53**, 21–26.

ROTH, M., COWAN, T. E., KEY, M. H., HATCHETT, S. P., BROWN, C., FOUNTAIN, W., JOHNSON, J., PENNINGTON, D. M., SNAVELY, R. A., WILKS, S. C. *et al.* 2001 Fast ignition by intense laser-accelerated proton beams. *Phys. Rev. Lett.* **86**, 436–439.

RUS, B., BATYSTA, F., ČÁP, J., DIVOKÝ, M., FIBRICH, M., GRIFFITHS, M., HALEY, R., HAVLÍČEK, T., HLAVÁC, M., HŘEBÍČEK, J. *et al.* 2011 Outline of the ELI-Beamlines facility. In *Diode-Pumped High Energy and High Power Lasers; ELI: Ultrarelativistic Laser-Matter Interactions and Petawatt Photonics; and HiPER: the European Pathway to Laser Energy* (ed. L. O. Silva, G. Korn, L. A. Gizzi, C. Edwards & J. Hein), vol. 8080, pp. 163–172. International Society for Optics and Photonics, SPIE.

SANTALA, M. I. K., ZEPF, M., BEG, F. N., CLARK, E. L., DANGOR, A. E., KRUSHELNICK, K., TATARAKIS, M., WATTS, I., LEDINGHAM, K. W. D., MCCANNY, T. *et al.* 2001 Production of radioactive nuclides by energetic protons generated from intense laser-plasma interactions. *Appl. Phys. Lett.* **78** (1), 19–21.

SCHWOERER, P. S., JÄCKEL, O., AMTHOR, K. U., LIESFELD, B., ZIEGLER, W., SAUERBREY, R., LEDINGHAM, K. W. D. & ESIRKEPOV, T. Z. 2006 Laser-plasma acceleration of quasi-monoenergetic protons from microstructured targets. *Nature* **439**, 445–448.

SENTOKU, Y., LISEIKINA, T. V., ESIRKEPOV, T. Z., CALIFANO, F., NAUMOVA, N. M., UESHIMA, Y., VSHIVKOV, V. A., KATO, Y., MIMA, K., NISHIHARA *et al.* 2000 High density collimated beams of relativistic ions produced by petawatt laser pulses in plasmas. *Phys. Rev.* E **62**, 7271–7281.

SIEGMAN, A. E. 1986 *Lasers*. University Science Books.

SNYDER, J., JI, L. L., GEORGE, K. M., WILLIS, C., COCHRAN, G. E., DASKALOVA, R. L., HANDLER, A., RUBIN, T., POOLE, P. L., NASIR, D. *et al.* 2019 Relativistic laser driven electron accelerator using micro-channel plasma targets. *Phys. Plasmas* **26** (3), 033110.

SOKOLLIK, T., PAASCH-COLBERG, T., GORLING, K., EICHMANN, U., SCHNÜRER, M., STEINKE, S., NICKLES, P. V., ANDREEV, A. & SANDNER, W. 2010 Laser-driven ion acceleration using isolated mass-limited spheres. *New J. Phys.* **12** (11), 113013.

STEINKE, S., BIN, J. H., PARK, J., JI, Q., NAKAMURA, K., GONSALVES, A. J., BULANOV, S. S., THÉVENET, M., TOTH, C., VAY, J.-L. *et al.* 2020 Acceleration of high charge ion beams with achromatic divergence by petawatt laser pulses. *Phys. Rev. Accel. Beams* **23**, 021302.

https://doi.org/10.1017/S0022377820000379 Published online by Cambridge University Press

STRICKLAND, D. A. & MOUROU, G. 1985 Compression of amplified chirped optical pulses. *Opt. Commun.* **56** (3), 219–221.

TOKITA, S., OTANI, K., NISHOJI, T., INOUE, S., HASHIDA, M. & SAKABE, S. 2011 Collimated fast electron emission from long wires irradiated by intense femtosecond laser pulses. *Phys. Rev. Lett.* **106**, 255001.

TOKITA, S., SAKABE, S., NAGASHIMA, T., HASHIDA, M. & INOUE, S. 2015 Strong sub-terahertz surface waves generated on a metal wire by high-intensity laser pulses. *Sci. Rep.* **5**, 8268.

WANG, J., HO, Y. K., KONG, Q., ZHU, L. J., FENG, L., SCHEID, S. & HORA, H. 1998 Electron capture and violent acceleration by an extra-intense laser beam. *Phys. Rev.* E **58**, 6575–6577.

WANG, P. X., HO, Y. K., YUAN, X. Q., KONG, Q., CAO, N., SESSLER, A. M., ESAREY, E. & NISHIDA, Y. 2001 Vacuum electron acceleration by an intense laser. *Appl. Phys. Lett.* **78** (15), 2253–2255.

WANG, W. M., CHEN, L. M., MAO, J. Y., HUANG, K., MA, Y., ZHAO, J. R., ZHANG, L., YAN, W. C., LI, D. Z., MA, J. L. *et al.* 2013 Collimated quasi-monoenergetic electron beam generation from intense laser solid interaction. *High Energy Density Phys.* **9** (3), 578–582.

WILKS, S. C., LANGDON, A. B., COWAN, T. E., ROTH, M., SINGH, M., HATCHETT, S., KEY, M. H., PENNINGTON, D., MACKINNON, A. & SNAVELY, R. A. 2001 Energetic proton generation in ultra-intense lasersolid interactions. *Phys. Plasmas* **8** (2), 542–549.

YOGO, A., BULANOV, S. V., MORI, M., OGURA, K., ESIRKEPOV, T. Z., PIROZHKOV, A. S., KANASAKI, M., SAKAKI, H., FUKUDA, Y., BOLTON, P. R. *et al.* 2015 Ion acceleration via 'nonlinear vacuum heating' by the laser pulse obliquely incident on a thin foil target. *Plasma Phys. Control. Fusion* **58** (2), 025003.

YOGO, A., DAIDO, H., BULANOV, S. V., NEMOTO, K., OISHI, Y., NAYUKI, T., FUJII, T., OGURA, K., ORIMO, S., SAGISAKA, A. *et al.* 2008 Laser ion acceleration via control of the near-critical density target. *Phys. Rev.* E **77**, 016401.

YOGO, A., MIMA, K., IWATA, N., TOSAKI, S., MORACE, A., ARIKAWA, Y., FUJIOKA, S., JOHZAKI, T., SENTOKU, Y., NISHIMURA, H. *et al.* 2017 Boosting laser-ion acceleration with multi-picosecond pulses. *Sci. Rep.* **7**, 42451.

ZAMFIR, N. V. 2012 The ELI-nuclear physics project. *J. Phys.: Conf. Ser.* **366**, 012052.

ZHU, L. J., HO, Y. K., WANG, J. X. & KONG, Q. 1998 Violent acceleration of electrons by an ultra-intense pulsed laser beam. *Phys. Lett.* A **248** (5), 319–324.

ZOU, J. P., LE-BLANC, C., PAPADOPOULOS, D. N., CHERIAUX, G., GEORGES, P., MENNERAT, G., DRUON, F., LECHERBOURG, L., PELLEGRINA, A., RAMIREZ, P. *et al.* 2015 Design and current progress of the Apollon 10 PW project. *High. Power Laser Sci. Eng.* **3**, doi:10.1017/hpl.2014.41.

https://doi.org/10.1017/S0022377820000379 Published online by Cambridge University Press